LA-UR-17-28776
Approved for public release; distribution is unlimited.

Title: Development of an ejecta particle size measurement diagnostic based on Mie scattering

Author(s): Schauer, Martin Michael
Buttler, William Tillman
Frayer, Daniel K.
Grover, Michael
LaLone, Brandon M.
Monfared, Shabnam Kalighi
Stevens, Gerald D.
Stone, Benjamin J.
Turley, William Dale

Intended for: Report

Issued: 2017-09-27

Development of an ejecta particle size measurement diagnostic based on Mie scattering

M. M. Schauer,[1] W. T. Buttler,[1] D. K. Frayer,[2] M. Grover,[3] B. M. LaLone,[3] S. K. Monfared,[1]
G. D. Stevens,[3] J. B. Stone[1] and W. D. Turley,[3]
[1]*Los Alamos National Laboratory, Los Alamos, NM 87545*
[2]*National Security Technologies, Los Alamos, NM 87544*
[3]*National Security Technologies, Special Technologies Laboratory, Santa Barbara, CA 93117*

I. INTRODUCTION

The goal of this work is to determine the feasibility of extracting the size of particles ejected from shocked metal surfaces (ejecta) from the angular distribution of light scattered by a cloud of such particles. The basis of the technique is the Mie theory of scattering, and implicit in this approach are the assumptions that the scattering particles are spherical and that single scattering conditions prevail. The meaning of this latter assumption, as far as experimental conditions are concerned, will become clear later.

The solution to Maxwell's equations for spherical particles illuminated by a plane electromagnetic wave was derived by Gustav Mie more than 100 years ago [1], but several modern treatises discuss this solution in great detail (e.g. [2]). The solution is a complicated series expansion of the scattered electric field, as well as the field within the particle, from which the total scattering and absorption cross sections as well as the angular distribution of scattered intensity can be calculated numerically. The detailed nature of the scattering is determined by the complex index of refraction of the particle material as well as the particle size parameter, x, which is the product of the wavenumber of the incident light and the particle radius, i.e. $x = 2\pi r/\lambda$.

Figure 1 shows the angular distribution of scattered light for different particle size parameters and two orthogonal incident light polarizations as calculated using the Mie solution. It is obvious that the scattering pattern is strongly dependent on the particle size parameter, becoming more forward-directed and less polarization-dependent as the particle size parameter increases. This trend forms the basis for the diagnostic design.

II. DIAGNOSTIC DESIGN

A. Experiment Packages

In the diagnostic development experiments described here, a thin sheet of ejecta was traversed by a collimated laser beam, and the scattered light intensity was measured at a number of different angles relative to the undeflected beam at zero degrees [21]. The relatively low levels of light predicted to be scattered by the ejecta led us to choose photomultiplier tubes (PMTs) for the scattered light detectors, and the need to separate these detectors from the explosive environment dictated that we use fiber-coupled light collectors of some sort. The eventual design comprised fiber-pigtailed collimators manufactured by OzOptics, Inc., epoxied into a delrin cylinder with an inner diameter of 76 mm surrounding the ejecta cloud and 2 meter-long optical fibers carrying the signal from the collimators out of the explosives confinement vessel. This cylinder and the explosively-driven metal target from which the ejecta were evolved were enclosed in a delrin and acrylic vessel which could be evacuated or pressurized.

Figure 2 is a schematic layout of an experiment package. In this view the CW laser beam enters from the right and any light scattered from the ejecta is collected by the fiber-coupled collimators on the left side of this view and transmitted to individual PMTs, the inputs of which contain narrowband filters with a passband width of 10 nm centered at 638 nm and better than 95% transmission at passband center. The output of each PMT is fed to a 12 bit digitizer with 2.5 ns time resolution resulting in a continuous trace of the scattered intensity as a function of time at each measurement angle. In addition, the unscattered laser beam is collected by a collimator at 0° in order to measure total light transmission through the cloud. Figure 3 shows an assembled experimental package.

The choice of angles at which the scattered light is sampled is dictated by the limitation imposed by the physical size of the collimators and the desire to maximize coverage of the expected scattered light pattern. As evident from Fig. 1, measurements on clouds of particles with size parameter greater than 3 must sample angles smaller than 30° but need not preserve light polarization.

Results from the holography experiments of Sorenson,*et al.*,[3, 4] showing particles with radii of a few microns led us to expect size parameters in the range of 10-20 for our laser wavelength, $\lambda = 638$ nm, dictating use of the smallest collection angles possible. Over many experiments, we have used several different angular arrangements to probe these particle clouds with the smallest measurement angle as low as 2° and the largest angle extending out to 75°.

As described later in this document, these experiments indicate that the relevant particle radii are actually less than 1 micron with size parameters most likely in the range of 3 to 10, which would seem to somewhat relax the requirement for small-angle measurements. However,

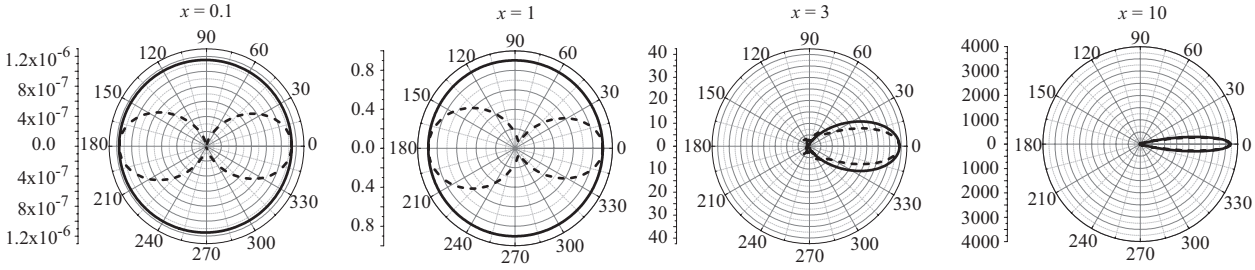

FIG. 1: Angular scattering intensity is shown for particles with 4 different size parameters. Solid lines are the scattering patterns produced when the incoming light is polarized perpendicular to the scattering plane and the dashed lines when parallel. The scattering plane is determined by the wave vector of the incident light and the position of the detector. Note also the increasing amplitude of the scattered intensity as the particle size increases as indicated by the vertical scale.

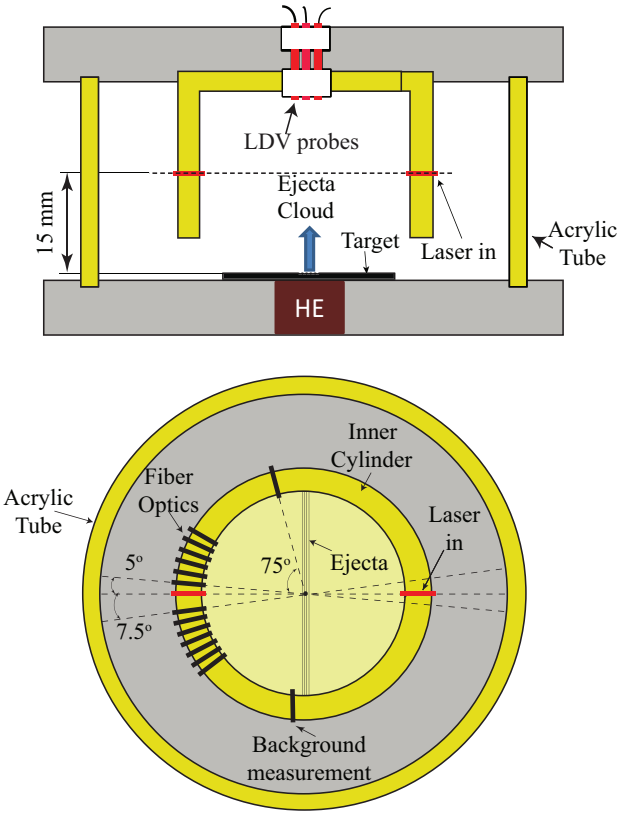

FIG. 2: Cross-sectional view of experiment package (upper panel) and layout of laser beam inlet and fiber-pigtailed collimators for collecting scattered light (lower panel).

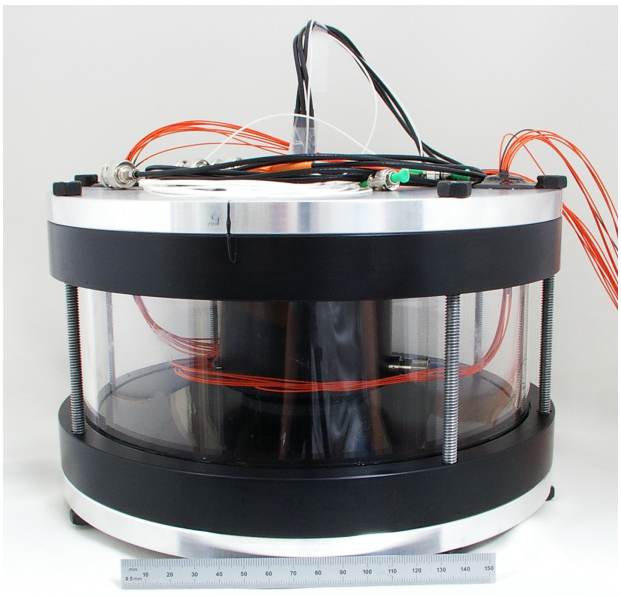

FIG. 3: Picture of an assembled experimental package showing the inner delrin cylinder into which the fiber-pigtailed collimators are epoxied.

it is still advantageous to acquire data at the smallest angles possible, so based on these anticipated sizes and the analysis of Howard, *et al.*, [5] our most recent measurements were conducted on two different package designs, one consisting of 6 measurement angles ranging from 4° to 29° in 5° steps with a complementary set of 6 measurement angles from −5° to −30°, also in 5° increments. A second design used a larger delrin cylinder (ID 127 mm) with five angles ranging from 2.5° to 16.5° in 3.5° increments with a complementary set starting at −3° and extending to −17° in the same 3.5° increments. Any change in experiment parameters such as target material or drive strength may require re-evaluation of the measurement angles used.

The much higher intensity, CW light in the transmitted beam was collecterd by a collimator at 0° and, in some cases, attenuated by neutral density (ND) filters before being fed to a photodiode. The ND filters ensured that the photodiode operated in its linear response region. The output from the photodiode was measured by a 12 bit digitizer.

The ejecta particles were produced by the interaction of an explosively-driven shockwave with periodic, triangular perturbations machined into the surface of Sn target wafers. The target was mounted to the black delrin

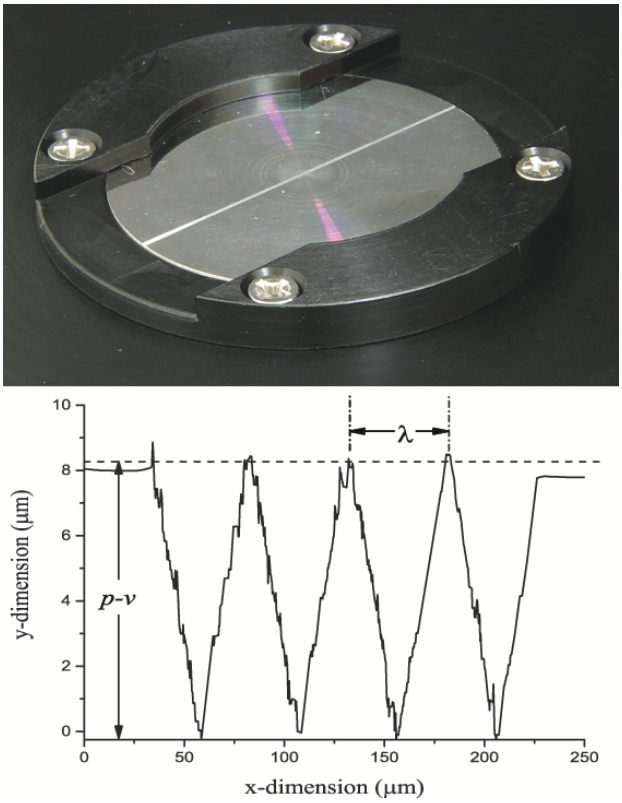

FIG. 4: Sn target mounted in the bottom plate of the experiment package (upper panel) and the profile of the target perturbations.

base plate of the experimental package shown in Fig. 3, and the HE charge was placed underneath the target in this base plate.

The upper panel of Fig. 4 shows such a target with a 200 μm wide set of triangular perturbations with a period, λ, of 50 μm and amplitude, h_0, of 4 μm mounted in the base plate of an experiment package. The lower panel is a lineout across the perturbation strip measured by optical profilometry. It is convenient to characterize the targets by the product of the wave number, $k \equiv \frac{2\pi}{\lambda}$ and the amplitude, h_0 of the triangular perturbations machined into the target surface. For this target $kh_0 = 0.5$.

The laser beam intersected the ejecta sheet at a height of 15 or 38 mm above target surface, depending upon the particular experiment series. In many, but not all, experiments quarter-millimeter-thick Ta masks with narrow slits, typically 750 μm in width, masked off all but a small portion of the ejecta cloud from the laser beam. The reasons for this will become clear later.

The light transmission can be used to determine whether multiple scattering effects are significant. Before the ejecta particles reach the laser beam, the transmission signal collected at 0° is simply the unscattered, incident laser intensity. As the ejecta move into the laser beam, the intensity of this transmitted light begins to fall

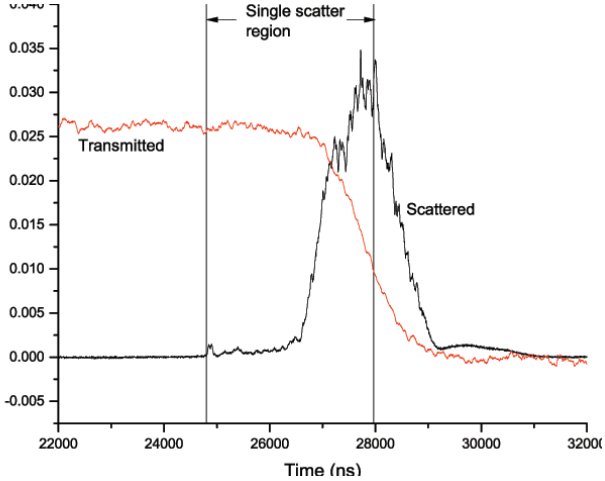

FIG. 5: Overlay of transmitted (red) and 5°, scaled scattered (black) intensity showing the region for which multiple scattering is deemed to have negligible effect.

due to scattering and absorption by the ejecta particles.

As long as the transmitted intensity is greater than $1/e$ times the quiescent level, we know from Beer's Law that the mean free path of a photon traversing the ejecta cloud is greater than the thickness of the cloud and multiple scattering effects can be neglected. This criterion serves as our definition of single scattering conditions, and we restrict our analysis to the scattering data from early in the experiment when this condtion is met.

Figure 5 shows an overlay of the intensity of the transmitted light and of that scattered into a collimator at 5° with respect to the unscattered beam. The time interval during which we deem the single-scattering assumption of the Mie theory to be valid is indicated by the two vertical lines just before 25000 ns and 28000 ns. Data outside of this region is not used. The scattered signal has been inverted and scaled down in this figure to enable display on the same scale as the transmitted signal.

In addition to measurements of scattered and transmitted light intensity, we measure the velocity of the free surface, v_{fs}, after shockwave breakout using laser Doppler velocimetry [7–12]. X-ray radiographs and nine-frame shadowgraphs are taken as additional diagnostic aids.

B. Detectors

It is essential that the detectors measuring the scattered and transmitted light operate in a region of linear response to the collected light power. Measurements on a subset of the PMTs used in these experiments showed linear responses up to laser powers producing 200 mV output signals into 50 Ω. Figure 6 shows the results of one of these measurements. The measurements were done using variable laser output power in 25 μs square pulses generated by a fiber-coupled acousto-optic modu-

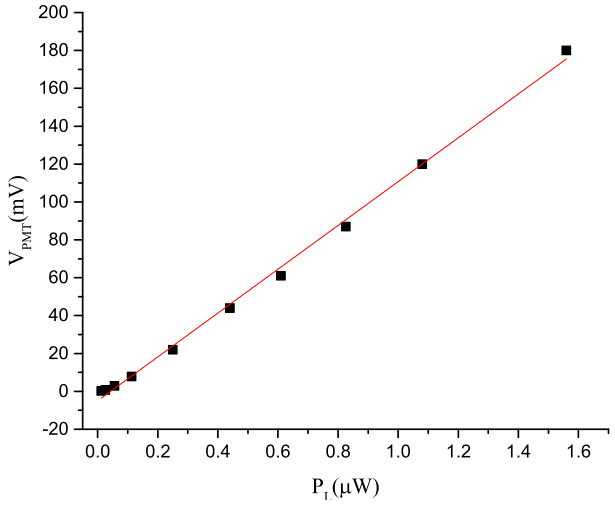

FIG. 6: Measurement of the response of one of the PMTs to varying incident laser light powers. The solid line is a linear fit to the data: $V_{PMT}(mV) = -4.9mV \pm 115.7\frac{mV}{\mu W} P_L(\mu W)$

lator (AOM) at a 100 Hz repetition rate. Signal levels during actual experiments can be restricted to the linear region by adjusting the output power of the 638-nm laser.

The sensitivity of individual PMTs will vary between different modules. In order to correct for this sensitivity variation in the measured, scattered light, we measure the sensitivity of each PMT before every experimental run using the same AOM-generated pulses as in the linearity measurments but with a fixed laser power. These measured sensitivities are normalized to a particular PMT, usually the one collecting light at the smallest angle, and the experimental data are corrected using these normalized sensitivities.

III. DATA ANALYSIS

A. Method

The measured intensity of scattered light at each angle is the sum of the contributions at that angle from all the particles within the scattering volume, which is determined by the overlap of the field of view of the collimator with the laser beam. The contribution of each individual particle to this sum is determined by its scattering amplitude, which is strongly size-dependent and can be calculated from the Mie solution as mentioned previously.

Hence, the scattered light intensity at angle θ_j, $I(\theta_j)$, is the sum of the scattering amplitude over all particles present in the sample with size parameters x_i, $|S(x_i, \theta_j)|^2$, multplied by the relative abundance in the sample, $f(x_i)$, of the particles characterized by that size parameter. That is,

$$\begin{bmatrix} I(\theta_1) \\ I(\theta_2) \\ I(\theta_3) \\ \vdots \\ I(\theta_N) \end{bmatrix} \propto \begin{bmatrix} |S(x_1,\theta_1)|^2 & |S(x_2,\theta_1)|^2 & |S(x_3,\theta_1)|^2 & \dots & |S(x_N,\theta_1)|^2 \\ |S(x_1,\theta_2)|^2 & |S(x_2,\theta_2)|^2 & |S(x_3,\theta_2)|^2 & \dots & |S(x_N,\theta_2)|^2 \\ |S(x_1,\theta_3)|^2 & |S(x_2,\theta_3)|^2 & |S(x_3,\theta_3)|^2 & \dots & |S(x_N,\theta_3)|^2 \\ \vdots & \vdots & \vdots & \ddots & \vdots \\ |S(x_1,\theta_N)|^2 & |S(x_2,\theta_N)|^2 & |S(x_3,\theta_N)|^2 & \dots & |S(x_N,\theta_N)|^2 \end{bmatrix} \begin{bmatrix} f(x_1) \\ f(x_2) \\ f(x_3) \\ \vdots \\ f(x_N) \end{bmatrix} \quad (1)$$

If only a single size of particle is present, then Eq. 1 is uniquely invertible, and the particle size can easily be extracted from the angular scattering pattern. If the particles are distributed over some range of sizes, then Eq. 1 is not uniquely invertible. Nevertheless, if additional information is available it may still be possible to constrain particle sizes.

As mentioned previously, holography data provides us with some guidance, and based on those results we restrict ourselves to particle radii less than 7 μm. In addition, the probability distribution function for this data appears to be well characterized by a log-normal distribution, so we assume that the particle radii in our experiments are also distributed log-normally. That is, the probability that an ejecta particle has a radius in the increment dr centered at r is

$$f(r; r_m, s)dr \equiv \frac{1}{\sqrt{2\pi}} \frac{1}{rs} e^{\frac{-[\ln(\frac{r}{r_m})]^2}{2s^2}} dr, \quad (2)$$

where the parameters of the distribution are the median radius, r_m, and a scale parameter, s, a unitless quantity that affects the shape of the distribution.

It is important to note that, unlike for a Gaussian distribution, the median and average are not the same for a log-normal distribution. In terms of the median radius and scale parameter the average radius is $\overline{r} = r_m e^{\frac{s^2}{2}}$. For small values of s, say less than 0.5, the distribution is nearly symmetric, and the average radius exceeds the median radius by less than about 10%. At $s = 1$, the average radius is 60% larger than the median radius. The standard deviation of the distribution, in terms of these quantities, is $\sigma = \overline{r}\sqrt{e^{s^2} - 1}$.

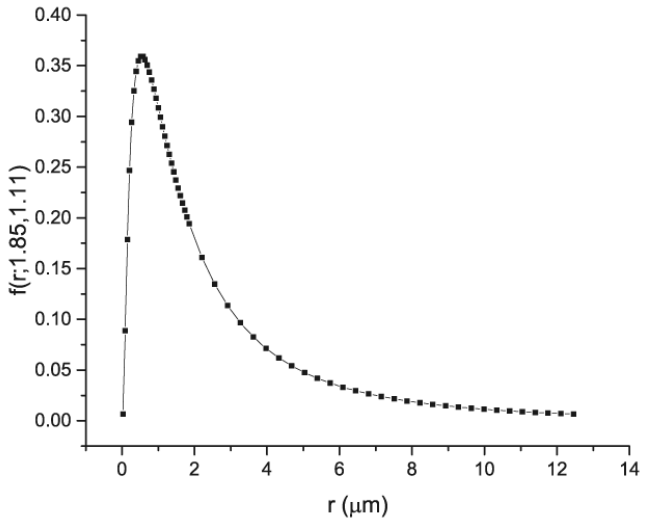

FIG. 7: A typical log-normal distribution. The squares are representative radii for which the scattering amplitude is calculated using the Mie solution.

For our analysis we choose N values of r_m and M values of s resulting in $N \times M$ possible distributions, typically starting with a coarse grid of values and refining the grid as the analysis proceeds. For each of these possibilities we choose a set of radii, r_j, that spans the distribution. Figure 7 shows the $f(r_j; r_m, s)$ for $r_m = 1.85$ μm and $s = 1.11$.

The angle-dependent scattered intensity for these radii is calculated using the Mie solution, and the sum of intensities over the entire set of radii, weighted by the abundance as given by the relevant log-normal distribution, is calculated for each angle. That is, the calculated, total, scattered intensity at a given angle, θ_i, is

$$I_{cal}(\theta_i; r_m, s) = \Sigma_j^K I_M(r_j, \theta_i) f(r_j; r_m, s), \qquad (3)$$

where $I_M(r_j, \theta_i)$ is the scattered intensity per unit incident intensity at θ_i from a particle of radius r_j calculated using the Mie solution; $f(r_j; r_m, s)$ is one of the $N \times M$ log-normal distributions; and the sum is over the K discrete values of r_j. This results in $N \times M$ calculated scattering patterns.

These calculated angular scattering patterns are used with the observed scattering pattern to form a reduced-χ^2 surface,

$$\chi^2 = [\Sigma_i^L (I_{obs}(\theta_i) - G * I_{cal}(\theta_i; r_m, s))^2 / \Omega_i^2] / \nu, \qquad (4)$$

in r_m, s, and G space. Here Ω_i is the uncertainty in the observed intensity, $I_{obs}(\theta_i)$; ν is the number of degrees of freedom of the data, essentially the number of angles, L, at which the measurements are made; and G is an overall scaling factor that is related to the system gain and the number of particles in the interaction volume.

The scattered intensity at each angle is sampled by the analysis routine a user-defined number of times throughout the time window for which single-scatter conditions are deemed to prevail as described earlier. The $I_{obs}(\theta_i)$ values used in Eq. 4 are the mean of the scattered intensity trace over a time window of 50 to 100 ns duration centered at each of the designated times, and the uncertainties in $I_{obs}(\theta_i)$ are the quadrature sum of the standard deviation of the mean and a contribution from the uncertainty in the PMT sensitivity measurements.

The minimum of the χ^2 surface yields the most probable values for the parameters r_m, s, and G at each sampled time, and the curvature of the surface about this point gives the uncertainty in these parameters (See for example [14]). In addition to the fit parameters the analysis routine returns the χ^2 value at this minimum, which serves as a monitor of the quality of the fit. In most cases the χ^2 values are close to one, indicating reasonable fits, but in a small number of shots an additional, constant uncertainty of about 1 mV, added in quadrature to the above-mentioned uncertainties, was needed to produce $\chi^2 \approx 1$. It is also true that some time points on particular traces fail to yield valid minima. That is, the χ^2 value appears to be decreasing at the extremes of one of the parameter values.

For example, if the minimum χ^2 value returned by the analysis routine corresponds to the minimum value of the scale parameter, it is impossible to know if this is a minimum or just another point along a decreasing line. Often, this problem can be addressed by expanding the range of fit parameters, i.e. by increasing the $N \times M$ possible distributions, but in some cases this is not physically possible requiring, perhaps, a negative scale parameter. Such points are discarded from the end results.

Finally, the resulting fits for each time are visually inspected by calculating the scattering pattern resulting from log-normally distributed particles with the returned fit parameters. These inspections are never used to reject points but help to determine if more work is needed on the data fits. All of this numerical work is done in Mathematica code.

B. Testing

As a first test of the data analysis method, we compare the scattering pattern calculated by the data analysis routine used here with MiePlot, freeware that is available on the web [13]. The input parameters to MiePlot are the median radius and the standard deviation of the distribution as a fraction of the median radius.

In Fig. 8, we compare patterns calculated by Mie plot and the Mathematica analysis routine for three different values of r_m with the standard deviation always the same fraction of that radius, while in Fig. 9 the median radius is kept fixed and the standard deviation is varied. Except for the case of the very smallest standard deviation, the MiePlot result is consistently lower than the result from the Mathematica code at zero degrees, but the two results agree reasonably well for angles greater than five degrees for all of the curves.

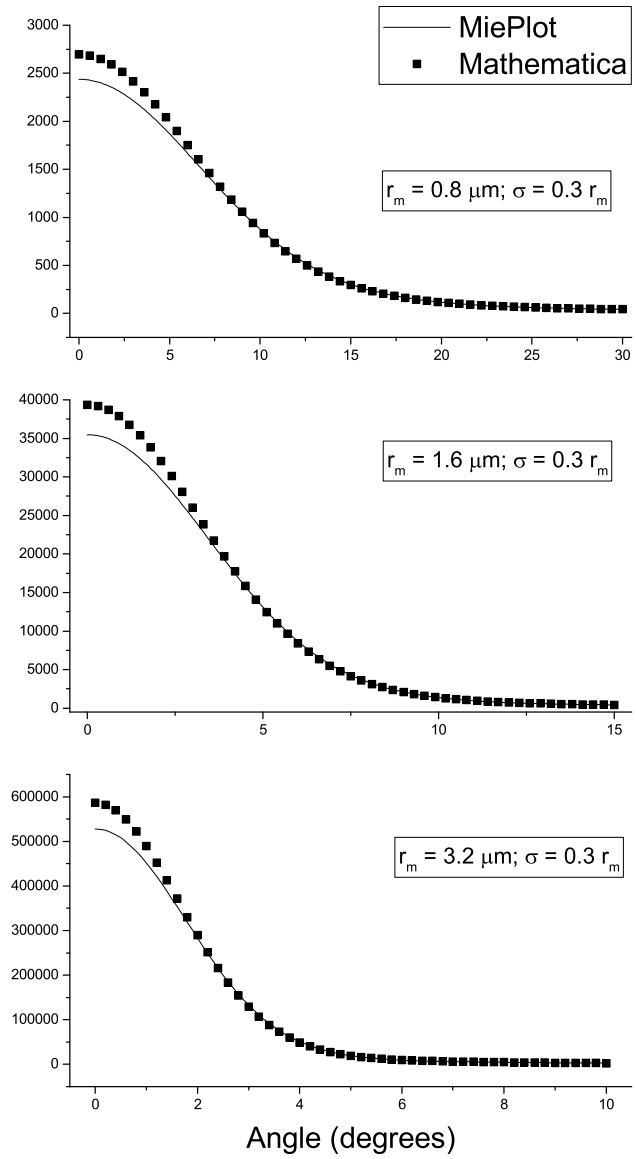

FIG. 8: Comparison of scattering patterns as calculated by MiePlot (solid line) and the analysis routine used for the work described here (squares). The median radius is varied and the standard deviation as a fraction of the radius is kept fixed. The values are indicated in the plots.

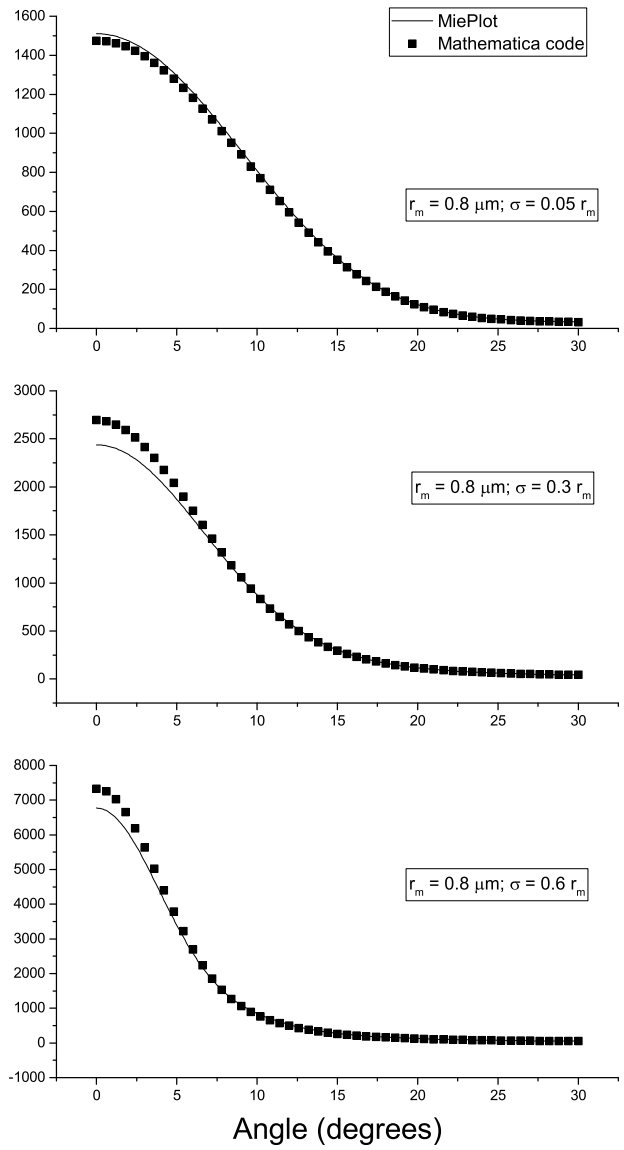

FIG. 9: Same as Fig. 8 but with the median radius kept fixed and the standard deviation varied.

Since most of the experiments we have conducted involve angles of four degrees or greater, this discrepancy would not result in a significant difference in the returned distribution parameters. However, the disagreement is not understood and raises concerns about the integrity of the fits. We continue to investigate this problem.

Further testing was done on synthesized data. Using typical experiment parameters, time traces were generated for a set of lognormal distributions with varying median radii and fixed scale parameter, s. Gaussian noise with a fixed width and Gaussian noise with width set to a percentage of the generated signal were added to the time traces. Figure 10 shows the resulting time trace for a detector at 4° with 0.3 mV baseline noise and 15% intensity noise added.

These time traces were then input to the analysis routine in exactly the same manner as actual Mie scattering data. The process was then repeated for synthesized data in which the median radius was kept fixed and the scale parameter was allowed to vary. The lower panel of Fig. 11 shows the median radius returned by the analysis routine as a function of the actual median radius used in the former test, while the upper panel shows the scale parameter returned by the routine as a function of actual median radius. Remember that the scale parameter was kept fixed throughout this exercise. Fig. 12 has the analogous plots for the scale parameter tests.

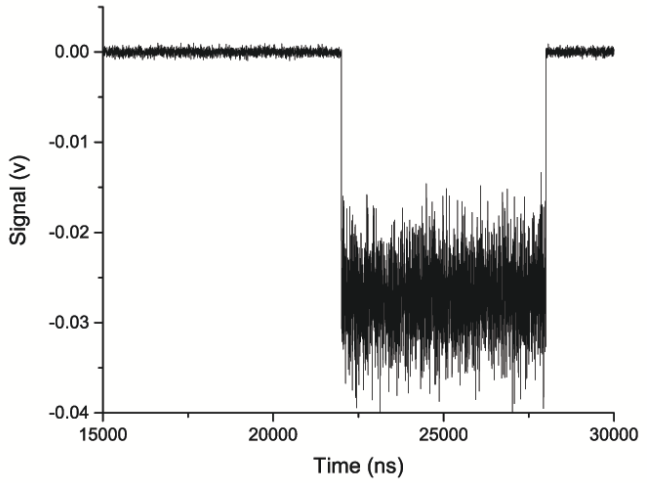

FIG. 10: Synthesized signal at 4° for a distribution of particles with median radius of 0.6 μm and scale parameter $s = 0.5$. Note that the signal is negative-going, consistent with the output of photomultiplier tube detectors.

IV. RESULTS AND DISCUSSION

A. General Discussion

As has already been stated, the $I(\theta)$ data are taken with a CW laser, so a continuous record of the scattering pattern is recorded from the moment the first ejecta arrive at the height of the interrogating laser beam until the collimators are destroyed by the arrival of the shockwave-driven target surface, the so-called free surface. The size distribution parameters, r_m and s, are then extracted from the scattering pattern, as described in the previous section, at any time within that window subject to the restriction imposed by the single-scatter criterion defined earlier.

Figure 13 shows the PMT signal versus time for five angles for a target with triangular grooves with 4 μm amplitude and 50 μm period ($kh_0 = 0.5$). These data have been corrected for differences in PMT sensitivity and inverted to give positive-going signals. Figure 14 shows the results of applying the fitting algorithm to that data at about 6 μs after the shockwave breaks out from the target surface. Figure 15 shows the r_m and s versus time for this target.

B. Comparison with Optical Holography Results

Comparison of the Mie scattering data with holography data is best accomplished by plotting the size versus the ratio of the velocity of the ejecta to the velocity of the free surface. Plotting the data in this manner rather than as a function of time removes shifts in time due to differences in the experiment geometries. Laser Doppler velocimetry is used to determine the velocity

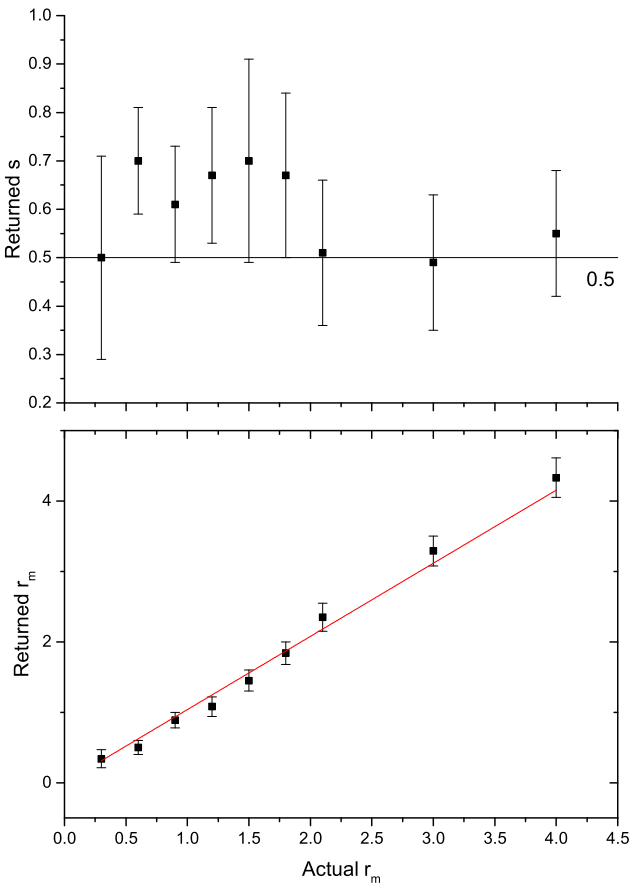

FIG. 11: Median radius (lower panel) and scale parameter (upper panel) returned by the data analysis routine for synthetic data in which the median radius was varied and the scale parameter kept fixed at 0.5. The solid line in the lower panel is a linear fit to the data with the intercept of the line fixed to zero. The resulting slope is 1.04 ± 0.03. The solid line in the upper panel is merely to guide the eye to the fixed value of the scale parameter.

of the shock-driven free surface simultaneously with the Mie scattering measurements of the angular scattering pattern, and the velocity of the ejecta is easily obtained from the time of the measured signal and the height of the laser beam above the target surface.

Although the Mie scattering data analysis routine returns the median radius, some holography data is given as median diameter while other data is given as average diameter. For log normal distributions these two quantities can be quite different. The average diameter of the log normal distribution is given by $2r_m Exp(\frac{s^2}{2})$ where r_m and s are the median radius and scale parameter, respectively, from the fitting procedure. This quantity will be more uncertain since the uncertainty in both r_m and s will contribute to the uncertainty of the average particle diameter. The quantity being plotted is clearly identified in the y-axis label and in the figure caption for each data plot that follows.

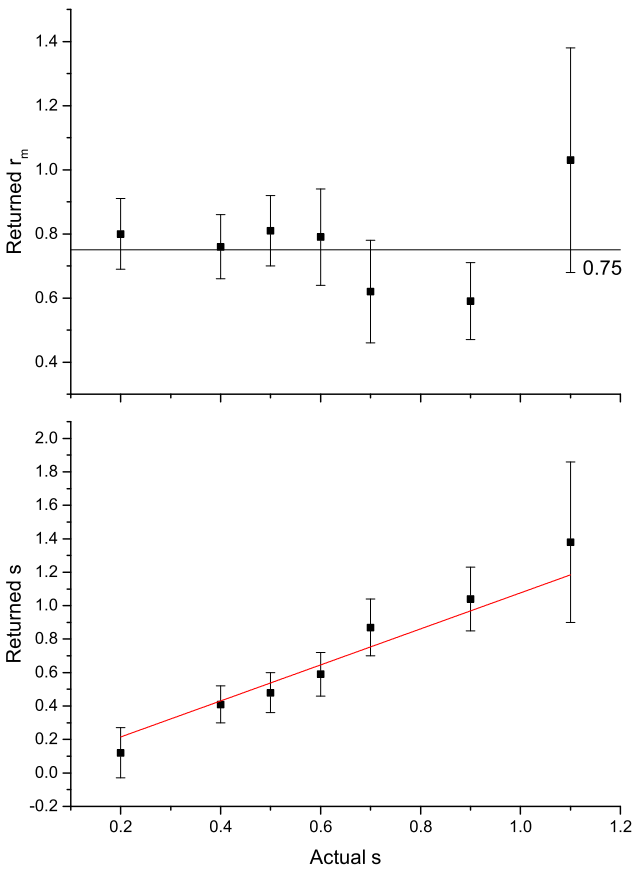

FIG. 12: Scale parameter (lower panel) and median radius (upper panel) returned by the data analysis routine in the case of fixed median radius of 0.75 μm.The solid line is a linear fit to the data with the intercept of the line fixed to zero. The resulting slope is 1.08 ± 0.07, while the solid line in the upper panel is, again, a guide for the eye.

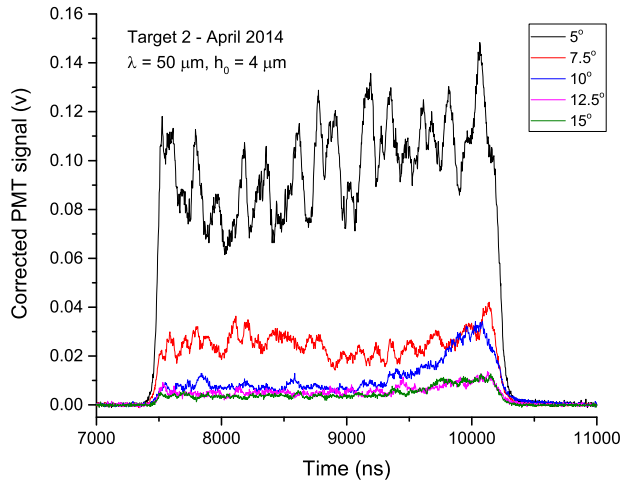

FIG. 13: Typical PMT signal levels vs. time from collimators at 5 different angles.

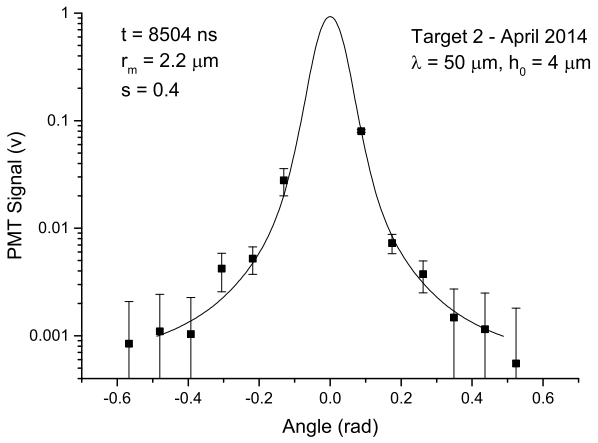

FIG. 14: Semilog plot of typical angular scattering pattern and the resulting fit.

Figure 16 shows a comparison of the median particle diameter for two different Mie scattering measurements to data from optical holography experiments [15, 16] on Sn targets that all have a single triangular groove with 40 μm depth and 120° degree opening angle. Although this groove is not periodic these parameters yield $kh_0 = 0.9$. The holography targets were 2 mm thick and were driven by half-inch diameter high-explosive (HE) pellets, while the Mie scattering targets for this data were 3 mm thick and were driven by one-inch diameter HE. These differences are not expected to lead to a significant difference in ejecta parameters.

The agreement between these data sets is good at high velocity ratios, but the holography data show a signficant increase in diameter at the lowest velocity ratios, i.e. at late times, while the Mie scattering data show no such trend. Numerical simulations [17, 18] of ejecta formation show ligaments evolving from the target surface features as the shock wave impinges on the surface. These ligaments stretch until a critical thickness is reached and the ligaments break up into individual particles. It is reasonable to surmise that such a process would tend to produce ejecta particles of uniform size throughout the cloud consistent with the results of the Mie scattering experiments. It is possible that the discrepancy between the two data sets at late times is due to multiple scattering effects or the presence of the ligaments complicating the analysis of the data.

We can also make comparisons of the average particle diameter as a function of He gas pressure as shown in Fig. 17. These data are all taken at $\frac{v_{ej}}{v_{fs}} = 1.5$ for single-groove targets. It should be pointed out that the two vacuum points in Fig. 17 (solid blue triangles) are from the same data as displayed in Fig. 16 but have been converted from median to average diameter.

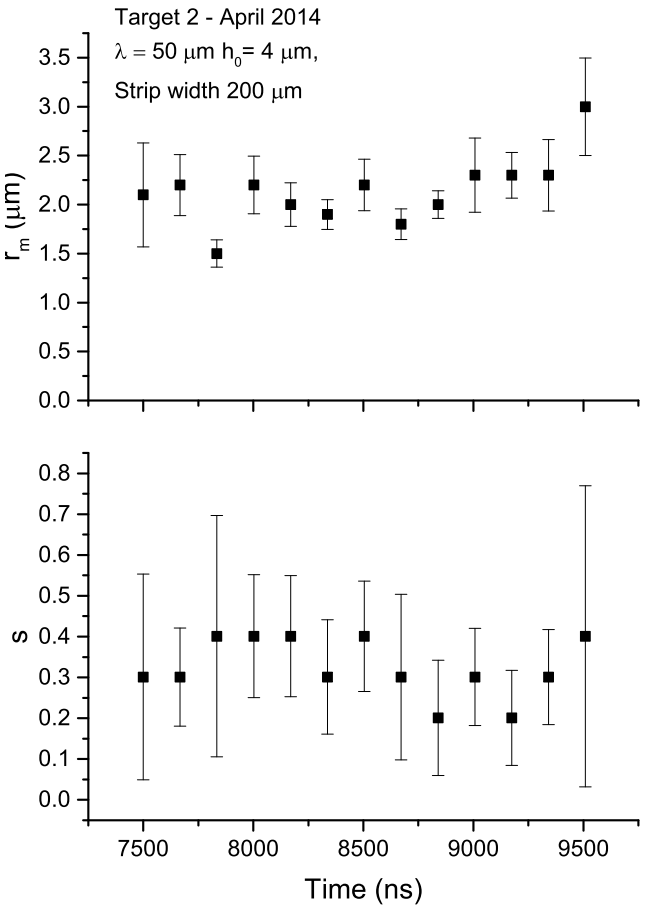

FIG. 15: The median radius and scale parameter as a function of time for the same target from which the data in figure 15 was taken.

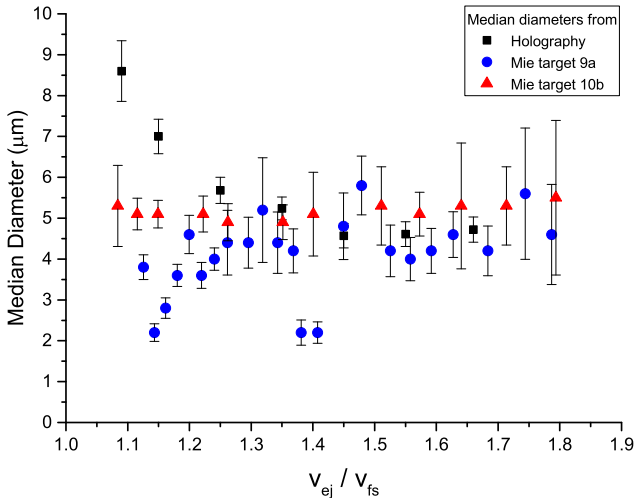

FIG. 16: The median diameter of ejecta as a function of ejecta velocity, v_{ej}, divided by the velocity of the free surface, v_{fs}. Data from optical holography (squares) are compared to two Mie scattering measurements (triangles and circles). All data in this figure are from targets with a single 40 μm deep groove 140 μm wide at the target surface.

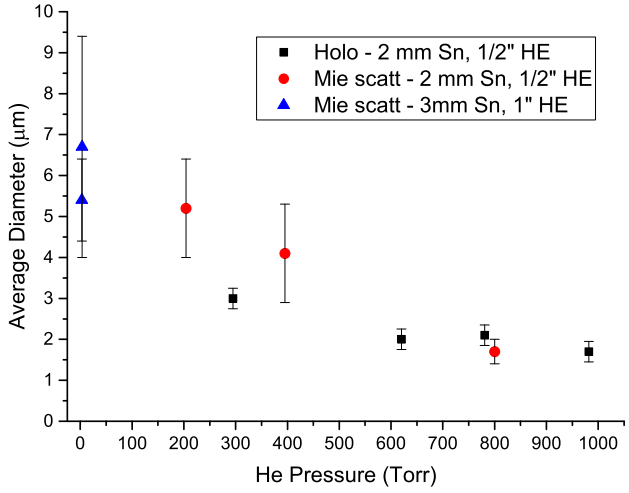

FIG. 17: The average diameter of ejecta as a function of He gas pressure from holography data (squares) and Mie scattering data (circles).

C. Edge Effects

As mentioned in section II X-ray images of the target and ejecta were also taken on most shots. These images show distinct differences in transmission at the edges of the ejecta clouds and non-uniformities in the expanding target material. The lower panel of Fig. 18 is an x-ray image of a Sn target with $kh_0 = 0.9$ as before but now with a 4 mm wide perturbation strip, i.e not a single groove.

The radiograph shows markedly decreased x-ray transmission at the edges of the ejecta cloud and significantly increased transmission through the material of the expanding target at the edges of the perturbation strips. These "cavitation waves" in the target material result from the interaction of the shockwave with the edges of the perturbation strip where the surface transitions from the periodic grooves to the diamond-turned finish of the remainder of the target surface.

It cannot be determined from x-ray images whether the decreased transmission at the edges of the ejecta cloud is due to the increased scattering cross section of larger particles than those present within the interior of the ejecta cloud or is due to more particles of the same size scattering light or to some combination of these two possibilities. It does seem clear that the bulk of the particles at the edges of the ejecta cloud come from material effected by the cavitation waves, while those in the center of the cloud come from the target perturbations.

Since one of the goals of the ejecta research program at LANL is to elucidate the role of surface features on ejecta production, it is desirable to remove the uncontrolled effects of the edges from the experimental results. To this end, we conducted experiments in which a mask with a slit much smaller in width than the perturbation strip width was placed between the target and the laser

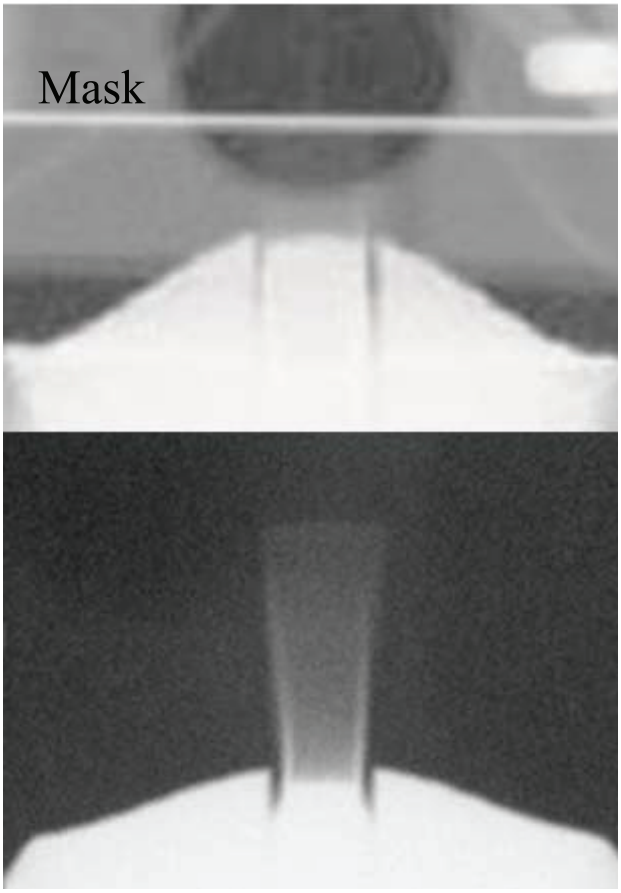

FIG. 18: X-ray radiographs of the evolving free surface of the shock-driven target and resulting ejecta cloud for an experiment with no mask (lower panel) and one with 0.25 mm thick Ta mask (upper panel).

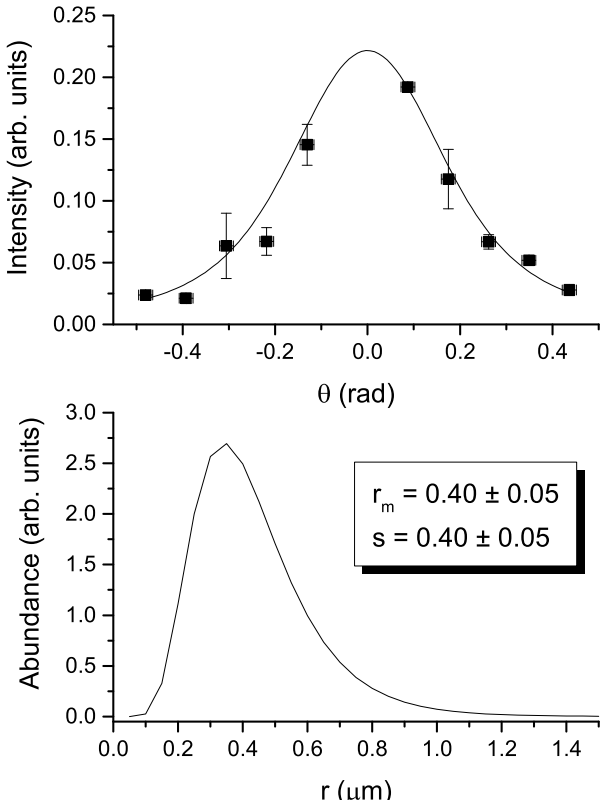

FIG. 19: Typical angular scattering data, fit (upper panel), and resulting log-normal size distribution (lower panel) for an experiment with a mask.

beam. All the data presented up to this point were taken without such masks.

The upper panel of Fig. 18 shows a 0.25 mm thick Ta mask with 0.75 mm wide slit above a Sn target with a 4 mm wide perturbation strip ($\lambda = 50$ μm, $h_0 = 4$ μm, $kh_0 = 0.5$). The slit in the mask is not visible in this image.

Figure 19 shows typical angular scattered intensity data and fit and the resulting size distribution for such an arrangement. The ejecta from the center of the perturbation strips are characterized by distributions with median radii that fall roughly in the range 200 nm $\leq r_m \leq 1$ μm as opposed to median radii of roughly 1 μm to 4 μm for experiments with no masks. Data from such experiments consistently yield smaller particle sizes than data from those experiments without masks.

Plots of r_m and s versus time for two different experiments in which masks were used are shown in Figs. 20 and 21. The targets used in these two experiments both had 3 mm wide perturbation strips with triangular perturbations with 50 μm period but different amplitudes as noted in the figure caption. The later times of these experiments relative to those shown in Figs. 15 are due to the increased height of the laser beam above the target surface necessitated by the intervening mask as well as the lower velocity of the ejecta produced by the smaller amplitude perturbations on these two targets. Both experiments used Ta masks with a 0.75 mm wide slit.

We have conducted many more experiments than the limited set presented here, and we consistently measure smaller ejecta particle sizes in experiments with masks than in those without, regardless of the details of the machined perturbations. From these data we conclude that the perturbations produce ejecta particles characterized by size distributions with median radii in the 200 nm to 1 μm range, while much larger particles with a less well controlled size distribution are evolved from the edges of the perturbation strips.

Thus, one would expect any experiment with no mask to produce an ejecta cloud with widely varying particle sizes. We often see large amounts of scatter in the measured particle size with time in experiments with no masks. Figure 22 shows data for one of the targets shown in Fig. 16 (target 9a) analyzed on a finer time grid. A large amount of scatter in the median radius and scale parameter is evident in this plot.

Curiously, the other Mie scattering target in Fig. 16 (target 10b) does not show an appreciable amount of

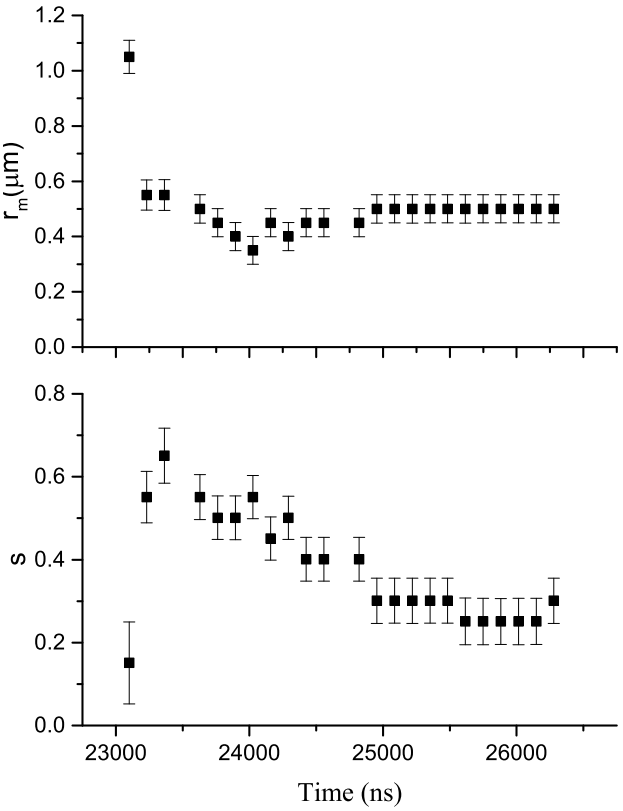

FIG. 20: Median radius and distribution width versus time for a target with perturbation with 50 μm period and 4 μm amplitude ($kh_0 = 0.5$) measured with intervening mask with a 0.75 mm slit.

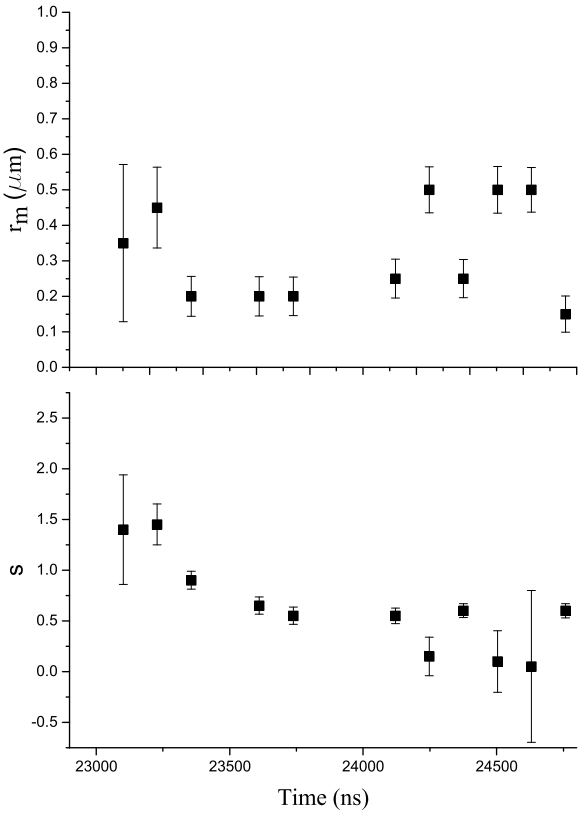

FIG. 21: Median radius and distribution width versus time for a target with perturbation with 50 μm period and 2.4 μm amplitude ($kh_0 = 0.3$) measured with intervening mask with a 0.75 mm slit.

scatter, although the targets were identical. Since the scattering cross section increases sharply with particle size (See Fig. 1), one would expect the larger particles in any cloud of ejecta to dominate the scattering. This effect may tend to wash out the signal from the smaller particles and, perhaps, smooth out the scatter in the measured cloud parameters.

It is worth noting here that targets with an "up-finish," i.e with the perturbations in the forms of ridges above the diamond-turned surface of the target rather than grooves into the surface, do not suffer from these cavitation effects [20]. Although such finishes are much more demanding to produce we have recently begun experiments with targets with up-finishes. It is too early to include the results of those experiments here.

D. Helium Gas Effects

Finally, we note that the presence of Helium gas seems to lead to a decrease in the scatter in particle sizes and push the distribution to smaller sizes, especially at the higher pressures that we have measured thus far. Figure 23 shows the median radius as a function of time for the Mie scattering experiments in Fig. 17 at 200, 400, and 800 torr of Helium gas pressure, and Fig. 24 shows the lognormal distributions calculated from the returned fit parameters at $\frac{v_{ej}}{v_{fs}} = 1.5$ for the vacuum data and the Helium gas data from Fig. 17. Broadly speaking, these observations are consistent with results from holography experiments conducted in gas, where the peak of the distribution is observed to move to smaller particle sizes as the gas pressure is increased [19].

The dramatic decrease in particle-size scatter with increasing gas pressure and the concomitant decrease in median radius to a stable value of about 600 nm is believed to be due to hydrodynamic breakup of the larger particles as they transport through the gas until a radius is reached for which the particles are hydrodynamically stable. The full implications of this preliminary data are still being investigated and more data is needed to confirm this result.

V. CONCLUSION

From these results we can draw several conclusions as to the viability of the Mie scattering technique in general

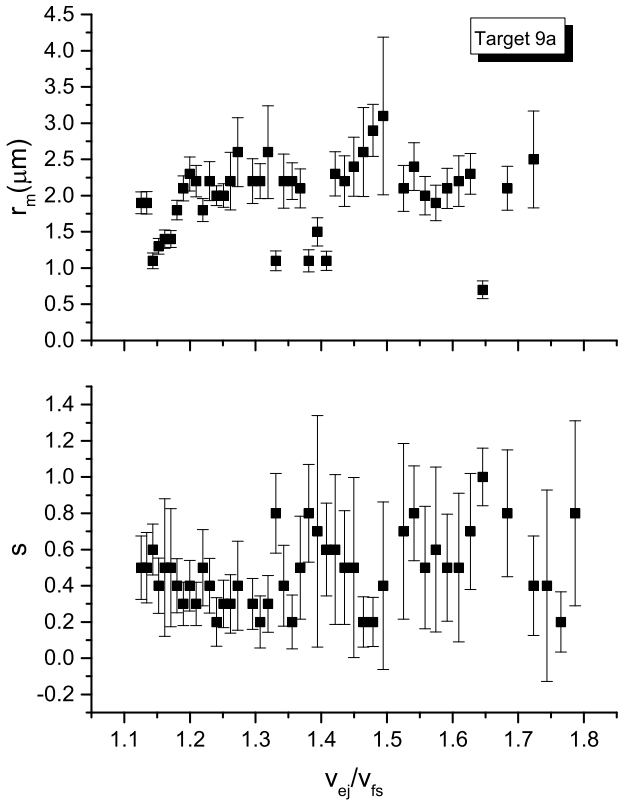

FIG. 22: Median radius and scale parameter for target 9a using a fine time grid for the analysis.

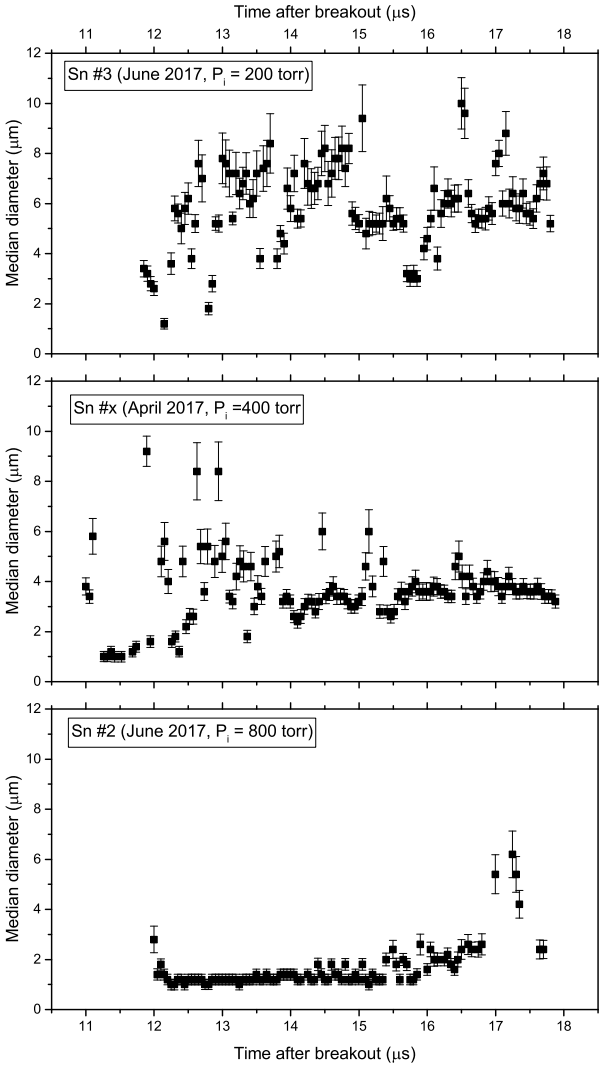

FIG. 23: Median radius as a function of time using a fine time grid for the analysis for three different Helium pressures as noted in the figure panels.

and ejecta phenomena in particular. It is obvious that the scattering technique as implemented here is extremely sensitive to the presence of ejecta, with high signal-to-noise ratio data available at very early times in these shock-driven experiments. It is also apparent that the technique will work not only in vacuum but also in the presence of some gases. We have successfully recorded Mie scattering signals up to Helium gas pressures of 3 atmospheres, but have not reported data above 1 atmosphere here due to problems with target hold-down rings used in the highest pressure experiments that call the interpretation of the data into question. The presence of certain gases may lead to fluorescence from the gas that would interfere with the Mie scattering signal, but no evidence of this has been seen to date.

The combination of the x-ray radiographs and the data from shots using masks, leads us to conclude that periodic surface features with $kh_0 \leq 0.9$ produce particles with median radii in the range of 200 nm to 1 μm, and shockwave interactions at the edges of these features produce much larger particles, with median radii ranging up to 5 μm. So far no systematic trend in particle size with respect to kh_0 has been detected, although the onset times of the Mie scattering signals show that surface features with higher kh_0 produce faster ejecta particles.

The data of Fig. 23, although preliminary, seems to indicate that, at least for certain metals and within a limited range of pressures, this diagnostic may be able to yield information on particle breakup times. It would seem that we would then be in a position to inform not only the source term for ejecta physics but also the transport process. Future work will investigate this possibility.

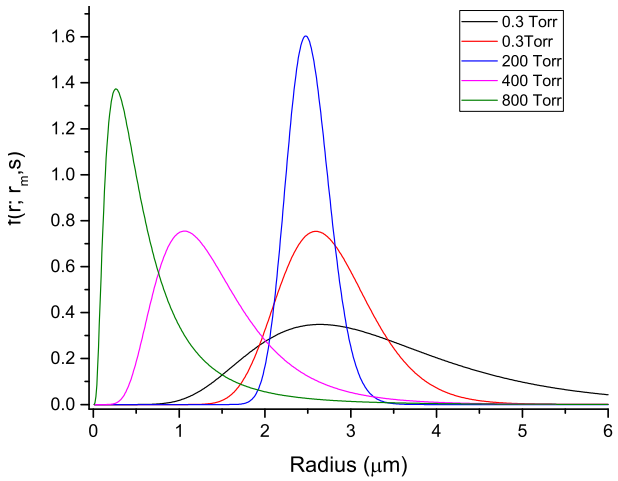

FIG. 24: Lognormal distributions as calculated from the fit parameters returned at $\frac{v_{ej}}{v_{fs}} = 1.5$ at the indicated pressures.

[1] G. Mie, "Contribution on the optics of turbid media, particularly colloidal metal solutions," Ann. der Physik **25**, 377–445 (1908).

[2] C. F. Bohren, D. R. Huffman, "Absorption and scattering of light by small particles," Chapter 13, WILEY-VCH Verlag GmbH & Co. KGaA, 2004.

[3] D. S. Sorenson, R. W. Minich, J. L. Romero, T. W. Tunnell and R. M. Malone, "Ejecta particle size distributions for shock-loaded Sn and Al targets," AIP Conf. Proc. **620**, 531–4 (2002).

[4] D. S. Sorenson, R. W. Minich, J. L. Romero, T. W. Tunnell and R. M. Malone, "Ejecta particle size distributions for shock-loaded Sn and Al metals," J. Appl. Phys. **92**, 5830–6 (2002).

[5] M. Howard, A. Luttman, D. Frayer, and D. Marks, "Mie Scattering Analysis," Unpublished report (2016).

[6] E.D. Palik and G. Ghosh, "Handbook of optical constants of solids," Academic Press, San Diego, 1998.

[7] H. Cummins, N. Knable, L. Gampel and Y. Yeh, "Frequency shifts in light diffracted by ultrasonic waves in liquid media," Appl. Phys. Lett. **2**, 62–64 (1963).

[8] H. Z. Cummins, N. Knable and Y. Yeh, "Spurious harmonic generation in optical heterodyning," Appl. Opt. **2**, 823–825 (1963).

[9] Y. Yeh and H. Z. Cummins, "Localized fluid flow measurements with an HeNe laser spectrometer," App. Phys. Lett. **4**, 176–178 (1964).

[10] J. W. Forman, Jr., E. W. George and R. D. Lewis, "Measurement of localized fluid flow velocities in gases with a laser *Doppler* flowmeter," Appl. Phys. Lett. **7**, 77–78 (1965).

[11] W. T. Buttler, S. K. Lamoreaux, F. G. Omenetto and J. R. Torgerson, "Optical velocimetry," arXiv:physics/0409073v1 (2004).

[12] O. T. Strand, D. R. Goosman, C. Martinez and T. L. Whitworth, "Compact system for high-speed velocimetry using heterodyne techniques," Rev. Sci. Instrum. **77**, 083108 (2006).

[13] www.philiplaven.com/mieplot.htm

[14] P.R. Bevington, "Data Reduction and Error Analysis for the Physical Sciences," McGraw-Hill, Inc. (1969) pp. 242-245.

[15] Sorenson DS, Minich RW, Romero JL, Tunnell TW and Malone RM (2002) Ejecta particle size distributions for shock-loaded Sn and Al targets. AIP Conf Proc 620:531–4.

[16] Sorenson DS, Minich RW, Romero JL, Tunnell TW and Malone RM (2002) Ejecta particle size distributions for shock-loaded Sn and Al metals. J Appl Phys 92:5830–6.

[17] Durand O and Soulard L (2015) Mass-velocity and size-velocity distributions of ejecta clouds from shock-loaded tin surface using atomistic simulations. J App Phys 117:165903.

[18] Cherne FJ, Hammerberg JE, Andrews MJ, Karkhanis V, and Ramaprabhu P (2015) On shock driven jetting of liquid from non-sinusoidal surfaces into vacuum. J App Phys 118:185901.

[19] Private communication from D. Sorenson.

[20] Private communication from W. Buttler.

[21] All scattering angles in this document are specified with respect to the forward direction of the undeflected laser beam.